Controlling Dzyaloshinskii-Moriya interactions in the skyrmion host candidates FePd$_{1-x}$Pt$_x$Mo$_3$N

Linus Kautzsch [1,2] Joshua D. Bocarsly [1,3,*] Claudia Felser,[2] Stephen D. Wilson,[1,3] and Ram Seshadri[1,3,4]

[1]*Materials Research Laboratory, University of California, Santa Barbara, California 93106, USA*
[2]*Max Planck Institute for the Chemical Physics of Solids, D-01187 Dresden, Germany*
[3]*Materials Department, University of California, Santa Barbara, California 93106, USA*
[4]*Department of Chemistry and Biochemistry, University of California, Santa Barbara, California 93106, USA*

Ferromagnets crystallizing in structures described by chiral cubic space groups, including compounds with the B20 or β-Mn structures, are known to host long-period chiral spin textures such as skyrmion lattices. These spin textures are stabilized by a competition between ferromagnetic exchange and antisymmetric Dzyaloshinskii-Moriya (DM) exchange, which is enhanced by the spin-orbit coupling associated with high-atomic-number elements. For real-world application, it is desirable to find materials that can host compact skyrmion lattices at readily accessible temperatures. Here, we report on the crystal chemistry and magnetic phase diagrams of a family of compounds with the filled β-Mn structure, FePd$_{1-x}$Pt$_x$Mo$_3$N, with T_C ranging from 175 to 240 K. DC and AC magnetization measurements reveal magnetic phase diagrams consistent with the formation of a skyrmion pocket just below T_C. The magnitudes of ferromagnetic and DM exchanges are determined from the phase diagrams, demonstrating that the introduction of increasing amounts of Pt can be used to increase spin-orbit coupling in order to control the expected skyrmion lattice parameter between 140 and 65 nm while simultaneously increasing T_C.

I. INTRODUCTION

Magnetic skyrmions are topologically protected vortex spin textures which act like single particles and may be manipulated as magnetic bits. These quasiparticle spin textures are promising candidates for magnetic racetrack memory and other low-power, high-density spintronic devices [1,2]. Magnetic skyrmions were first observed in B20 compounds (space group $P2_13$) MnSi [3] and Fe$_{0.5}$Co$_{0.5}$Si [4,5]. In this structure type, breaking of inversion symmetry generates long-range Dzyaloshinskii-Moriya (DM) exchange driven by spin-orbit coupling [6–8]. Competition between this antisymmetric exchange and the usual ferromagnetic exchange leads to stabilization of long-period chiral spin structures, including helimagnetic, conical, and skyrmion lattice states.

It is of particular interest to develop new materials that exhibit skyrmions near room temperature with small diameters of the skyrmion vortex. Most known bulk hosts form stable skyrmion lattices only in a small pocket in the temperature and field phase diagram just below the Curie temperature: around 30 K for both MnSi and Fe$_{0.5}$Co$_{0.5}$Si [9,10]. In order to stabilize skyrmions at higher temperatures, one must look to chiral magnets with high Curie temperatures (i.e., strong ferromagnetic exchange). In the B20 compound FeGe, which has $T_C = 278$ K, skyrmions have been observed near room temperature [11]. More recently, skyrmion lattices at temperatures at and above room temperature have been studied in the compounds Co$_x$Zn$_y$Mn$_z$ $(x + y + z = 20)$ with the β-manganese crystal structure (space group $P4_132$

or $P4_332$) [12]. As in the B20 compounds, these materials exhibit a stable skyrmion pocket just below T_C, which is tunable between about 150 and 475 K. Remarkably, by field cooling through this pocket, one may also observe a long-lived metastable skyrmion lattice which exists in a broad range of temperatures and fields [13,14]. This phenomenon is believed to be caused by pinning of the skyrmions by the atomic-site disorder [4,13–16].

The skyrmion lattice parameter is controlled by a balance between the ferromagnetic exchange, which supports parallel alignment of spins, and the DM exchange, which supports rotation of near-neighbor spins with respect to one another. The lattice parameter is therefore approximately given by $2\pi A/D$ [17], where A is the ferromagnetic exchange stiffness and D is the DM exchange density [6,18,19]. In principle, one may therefore decrease the skyrmion size by introducing heavy atoms into a skyrmion host to increase spin-orbit coupling and increase D. This approach has been successful in thin-film heterostructures, where adding a layer of a heavy element such as Pt next to a magnetic layer can tune spin-orbit coupling (SOC) [20]. However, in bulk materials, this approach has not been straightforward to implement because chemical substitutions of heavy elements tend to have the dominant effect of weakening ferromagnetic exchange stiffness A. This may result in smaller skyrmions, but at the cost of dramatically lowering the temperature at which the skyrmion lattice phase is observed. For example, in Mn$_{1-x}$Ir$_x$Si, the skyrmion lattice parameter decreases by a factor of two for $x = 0.06$, but the T_C decreases by a factor of three [21]. In Fe$_{1-x}$Mn$_x$Ge, a composition change of $x = 0.2$ decreases the skyrmion lattice parameter by a factor of four, while T_C decreases by roughly 20% [22].
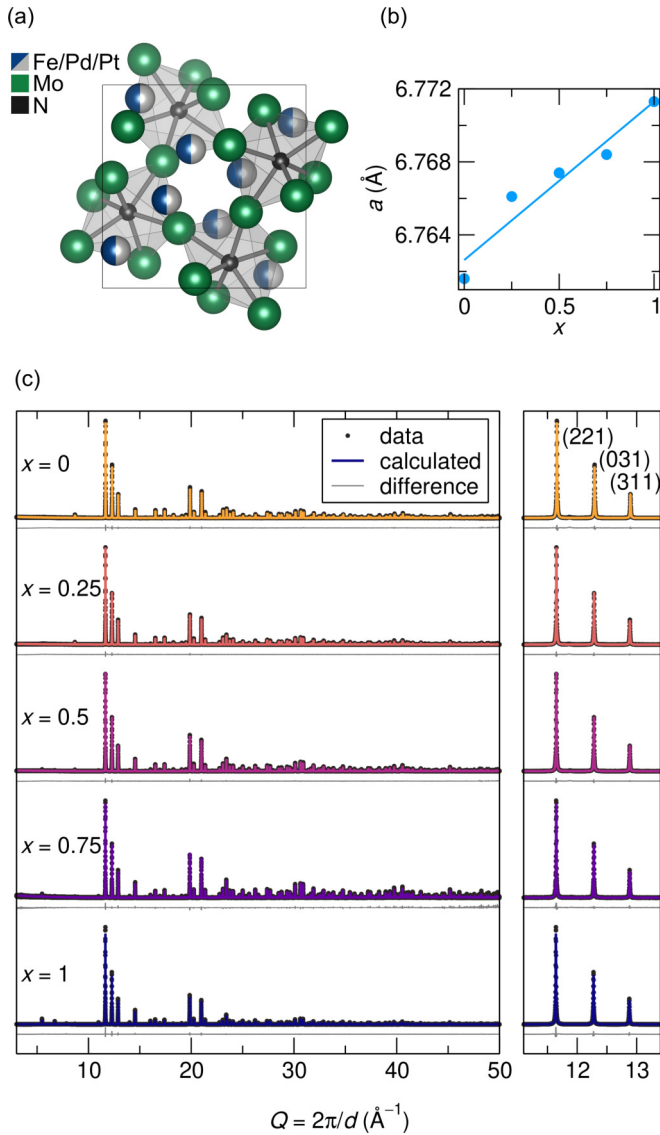
*jdbocarsly@mrl.ucsb.edu

(a)

(b)

(c)

FIG. 1. (a) Crystal structure of the cubic series $FePd_{1-x}Pt_xMo_3N$ (space group $P4_132$), shown projected down one of the cubic axes. The origin of the cell has been translated by 0.25 of a unit cell such that the chiral fourfold screw axis (4_1) is centered in the cell. (b) Evolution of the lattice parameter a as a function of x (error bars are smaller than the points). (c) Synchrotron diffraction pattern shown with Rietveld fits to the $P4_132$ β-Mn structure.

Battle and co-workers [23–26] have reported the formation of ferromagnetic nitrides in the filled-β-Mn structure $Fe_{2-x}M_xMo_3N$ (M = Co, Ni, Rh, Pd, Pt) with Curie temperatures up to 225 K (M = Pt). This structure type, shown in Fig. 1(a), is simply the β-Mn structure type with additional interstitial B, C, or N atoms. As these compounds have the chiral space groups of β-Mn ($P4_132$ or $P4_332$) and show ferromagnetic behavior, they are good candidates for skyrmion formation. Indeed, skyrmions in the filled β-manganese compound $Fe_xCo_{1.5-x}Rh_{0.5}Mo_3N$ at temperatures around 100 K have been reported using Lorentz transmission electron microscopy and magnetic measurements [27].

Here, we report the preparation of $FePd_{1-x}Pt_xMo_3N$ as a series with five compounds (x = 0, 0.25, 0.5, 0.75, 1)

and the characterization of their structural and magnetic properties. Magnetic phase diagrams are determined, revealing an A-phase pocket just below the Curie temperatures, which is expected to host a skyrmion lattice. An analysis of these phase diagrams shows that the introduction of Pt atoms, associated with large spin-orbit coupling, leads to an increase in D while leaving A largely unchanged. Therefore, this substitution dramatically lowers the expected skyrmion lattice parameter while actually enhancing T_C. This study demonstrates how the introduction of heavy atoms can be used to control chiral magnetism in a bulk material, in a system where such a substitution does not weaken ferromagnetic exchange.

II. METHODS

A. Sample preparation

Polycrystalline samples of $FePd_{1-x}Pt_xMo_3N$ (x = 0, 0.25, 0.5, 0.75, 1) were prepared by direct nitridation of the metals [28]. The appropriate transition metals were intimately ground in stoichiometric mixtures, pelletized, and heated under a gas flow of 5% H_2 in N_2 (flow rate $\approx$ 7 dm^3 min.$^{-1}$) for 36 h at 975 °C. The samples were then reground and repelletized and heated once again at the same conditions for 24 h. In both steps of the process, the furnaces were purged with the reaction gas prior to heating and the samples were cooled down to room temperature under gas flow. Samples with a total mass of 500 mg were prepared. Reagents employed were Fe (Sigma-Aldrich) 99.9%, Pd (Sigma-Aldrich) 99.9%, Pt (Alfa Aesar) 99.95%, and Mo (Sigma-Aldrich) 99.9%. This thermal treatment procedure gave well-crystalized phase-pure samples according to laboratory x-ray diffraction, but in order to further improve on the sample crystallinity and density, the samples were again reground and repelletized and annealed in amorphous silica tubes filled with 1 atm N_2 for 48 h. In order to contain this pressure and temperature of N_2 gas safely, thick-walled silica tubes were chosen (outer diameter 15.8 mm, wall thickness 2.8 mm, length $\approx$ 7 cm). The samples were annealed at the following temperatures: x = 0 at 1000 °C, x = 0.25 at 1050 °C, x = 0.5 at 1100 °C, x = 0.75 at 1150 °C, and x = 1 at 1200 °C. These annealing temperatures were chosen to be about 50 °C below the decomposition temperature of each sample, as determined by differential scanning calorimetry.

B. Characterization

The progress after each step of the synthesis was verified by x-ray powder diffraction using a Panalytical Empyrean powder diffractometer operating with Cu-K$_\alpha$ radiation in Bragg-Brentano geometry. Differential scanning calorimetry was performed using a Netzsch DSC 404 C Pegasus Thermal analyzer equipped with a high-temperature furnace (up to 1500 °C). Samples with a mass of about 20 mg were measured in Al_2O_3 crucibles in flowing N_2 gas. After successful preparation, high-resolution synchrotron powder-diffraction data were collected for all samples in the series at beamline 11-BM at the Advanced Photon Source (APS), Argonne National Laboratory, using an average wavelength of 0.457838 Å. The patterns were collected at a temperature of 295 K. Elemental

analysis was performed on powder samples on Kapton tape using a Rigaku ZSX Primus IV x-ray fluorescence (XRF) spectrometer.

Rietveld refinement of the crystal structures was carried out using TOPAS academic. The synchrotron patterns were fit with a Stephens strain model [29] (two parameters) and a standard Gaussian size broadening term (one parameter). A fixed axial divergence asymmetry correction based on the instrument geometry was used to handle diffractometer peak asymmetry. Absorption of the x rays by the capillary samples was corrected for according to the chemical compositions and capillary diameter (0.8 mm) by refining the packing density of the samples to values between 30% and 40%. Unit-cell parameters, atom positions, as well as the elemental compositions were refined, assuming the atomic sites were each fully occupied. For the samples containing both Pd and Pt, the compositions were additionally restricted to stoichiometries consistent with the nominal Pd/Pt ratio, e.g., for $x = 0.25$: $x_{Pd} = 0.25(1 - x_{Fe})$ and $x_{Pt} = 0.75(1 - x_{Fe})$. Isotropic displacement parameters (B_{iso}) were refined for the two metal-filled sites in the unit cell. The value for the nitrogen-filled $4a$ site was fixed to a refined overall B_{iso}.

DC and AC magnetic measurements between 2 and 400 K were obtained on a Quantum Design MPMS3 SQUID magnetometer. Pieces with masses less than 1 mg were measured in polypropylene capsules. First, DC magnetization as a function of temperature between 2 and 400 K was collected under a constant field of 0.02 T while sweeping temperature at a rate of 7 K min^{-1}. Five-branch hysteresis loops between -7 and 7 T were then collected at 2 K at a rate of 10 mT s^{-1}. Detailed magnetic phase diagrams for the $x = 0$, 0.5, and 1 samples were constructed using DC magnetization and AC susceptibility measurements as a function of field at closely spaced temperatures near the magnetic transition. The AC susceptibility measurements were performed every 2 K at temperatures below the Curie transition using excitation frequencies of 10 Hz and amplitudes of 0.5 mT. The susceptibility was measured every 0.7 mT between 0 and 25 mT, and every 5 mT between 25 and 100 mT. The DC magnetization was measured every 1 K while sweeping at a rate of 0.2 mT s^{-1} between 0 and 100 mT, and collecting a data point every 1 second. The field derivatives of the AC and DC measurements were calculated using Tikhonov regularization [30].

Additionally, the magnetoentropic behavior of FePtMo$_3$N was characterized using the technique described in Ref. [31]. DC magnetization versus temperature sweeps at closely spaced fields were performed around the magnetic transition temperature of FePtMo$_3$N to obtain magnetocaloric information. The sweeps were performed between 210 and 240 K at a rate of 4 K min^{-1} with a spacing of 2 mT between 2 and 30 mT, and a spacing of 5 mT between 30 and 80 mT. The temperature derivatives of these sweeps were then calculated using Tikhonov regularization as well to give information about how the entropy changes with applied field at any given temperature and field, according to the Maxwell relation,

$$\left(\frac{\partial M}{\partial T}\right)_H = \left(\frac{\partial S}{\partial H}\right)_T, \tag{1}$$

TABLE I. Results of Rietveld refinement. Lattice parameter a; x coordinate of the $8c$ position; B_{iso} value of the $8c$ position; y coordinate of the $12d$ position; B_{iso} value of the $12d$ position; fraction x of Fe, Pd, and Pt on the $8c$ position; R factors R_{wp} and R_{exp}. Numbers in parentheses are standard uncertainties in the last given digit from Rietveld refinement. Uncertainties for the lattice parameters and atomic coordinates are smaller than the least significant figure shown.

x	0	0.25	0.5	0.75	1
a (Å)	6.762	6.766	6.767	6.768	6.771
$8c$ x	0.0654	0.0656	0.0654	0.0653	0.0650
$8c$ B_{iso}	0.91(2)	0.76(2)	0.68(1)	0.60(2)	0.90(1)
$12d$ y	0.2046	0.2045	0.2043	0.2042	0.2041
$12d$ B_{iso}	0.79(1)	0.68(1)	0.63(1)	0.47(2)	0.77(7)
x_{Fe}	0.500(8)	0.500(5)	0.503(3)	0.501(5)	0.491(2)
x_{Pd}	0.500(8)	0.375(3)	0.248(1)	0.125(1)	
x_{Pt}		0.125(1)	0.248(1)	0.374(4)	0.509(2)
R_{wp}	21.02	18.95	16.56	29.04	15.93
R_{exp}	17.04	16.13	13.36	30.41	10.79

where M, T, S, and H are the magnetization, temperature, entropy, and field, respectively. This quantity can then be integrated with respect to field to give the isothermal magnetic entropy change $\Delta S_M(T, H)$, which is the entropy difference between the sample at a magnetic field H and at zero field,

$$\Delta S_M(T, H) = \int_0^H \left(\frac{\partial M}{\partial T}\right)_{H'} dH'. \tag{2}$$

III. RESULTS AND DISCUSSION

A. Crystal structure

Rietveld refinements of synchrotron powder-diffraction patterns for the compounds in the series FePd$_{1-x}$Pt$_x$Mo$_3$N are shown in Fig. 1(c). The reported β-Mn structure ($P4_1 32$) [28] fits the obtained diffraction patterns very well. Sharp diffraction peaks are observed, and no peaks violating this model or suggesting the presence of secondary phases are observed. The $8c$ site is occupied by a combination of Fe, Pd, and Pt. Mo fully occupies the $12d$ site, forming distorted corner-sharing Mo$_6$N octahedra with the interstitial nitrogen atoms on the $4a$ site, as shown in Fig. 1(a). The lattice parameter of the unit cell is found to increase with rising Pt content; see Fig. 1(b). The refined compositions are in good agreement with the results from the XRF measurements (Table S1 in Supplemental Material [32]). Details of the refinements are presented in Table I.

Differential scanning calorimetry (DSC) was employed to characterize the thermal stability of the compounds after the two gas nitridation steps. Upon heating under 1 atm of N$_2$ gas, all samples show an endothermal signal somewhere between 1100 °C ($x = 0$) and 1250 °C ($x = 1$) (Fig. S1 of the Supplemental Material [32]), which corresponds to decomposition of the samples via loss of nitrogen. Upon subsequent cooling, the nitrogen is not reabsorbed and the resulting sample is found to be a mix of metal binaries. When heating in Ar, the decomposition temperatures were found to be
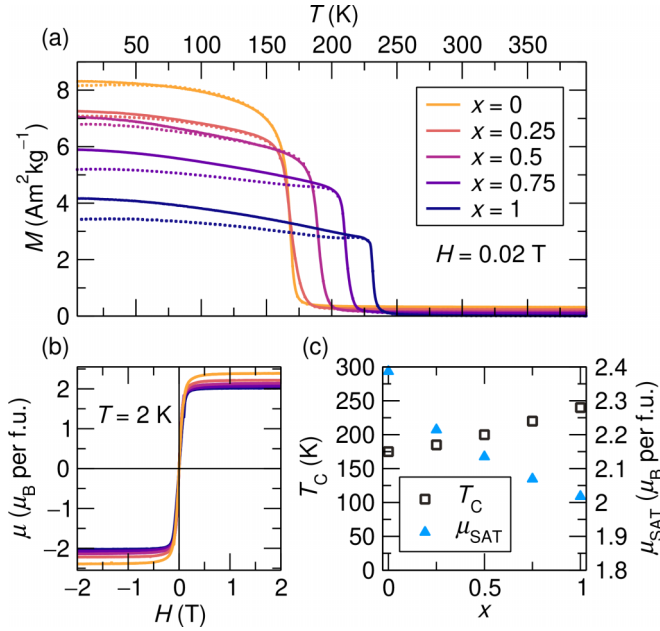
FIG. 2. (a) Magnetization as a function of temperature collected under an applied magnetic field of $H = 0.02$ T, collected while warming after either cooling under zero field (dotted line) or cooling under a field (solid line). (b) Magnetization as a function of the applied magnetic field at $T = 2$ K. (c) T_C and μ_{sat} as a function of x.

roughly 100 K lower, and so the annealing step for the sample preparation was performed under nitrogen pressure, using temperatures chosen to be about 50 K below the observed decomposition temperature of each sample. This annealing step is found to substantially improve sample crystallinity, as evidenced by narrow diffraction peak widths and the sharpness of the magnetic transitions. Because the $x = 1$ sample has the highest decomposition temperature, it could be annealed at the highest temperature and consequently has the clearest magnetic features.

B. Magnetic properties

All compounds of the series show soft ferromagnetic behavior and a saturated magnetic moment between 2.0 and 2.4 μ_B per Fe atom at $T = 2$ K [Fig. 2(b), Table II]. The magnetization saturates at approximately $H = 0.4$ T. This behavior is consistent with other reports on this materials class [24,25]. The zero-field-cooled warming and the field-cooled warming curves in Fig. 2(a) display a small amount of irreversibility below the Curie temperature, with

TABLE II. Curie temperature T_C and saturation magnetization μ_{sat} per Fe at $T = 2$ K and $H = 2$ T.

x	T_C (K)	μ_{sat} (μ_B/Fe)
0	175	2.39
0.25	185	2.21
0.5	200	2.14
0.75	220	2.07
1	240	2.02

the splitting between field-cooled and zero-field-cooled curves increasing with increasing Pt content. However, this irreversibility is too small to cause a visible hysteresis around the origin in the $M(H)$ hysteresis loops. The sharpness of the Curie transitions supports that the samples are of high quality. T_C was determined from the onset of the Curie transition.

C. Magnetic phase diagrams

Magnetic phase diagrams for the $x = 0$, 0.5, and 1 samples were constructed on the basis of DC magnetization and AC susceptibility measurements as a function of field, collected at several temperatures near the Curie temperature. This process is shown in detail for $FePtMo_3N$ ($x = 1$) in Fig. 3. Thirteen DC $M(H)$ curves and eight AC $\chi'(H)$ curves are shown. The AC susceptibility measurements are collected using a relatively low excitation frequency of 10 Hz, and therefore should approximately correspond to the field derivative of the DC magnetization data dM/dH. Therefore, the DC and AC data are expected to provide the same information, although measurement and data analysis details may lead to minor differences. In practice, we find that the AC measurements serve as a high-sensitivity complement to the high-density data derived from DC magnetization.

Just below $T = 230$ K, a characteristic double-bump feature may be seen in both AC $\chi'(H)$ [Fig. 3(d)] and in dM/dH calculated from the DC magnetization data [Fig. 3(b)]. This feature is characteristic of the phase evolution seen just below T_C in chiral cubic magnets [9,10,12,27,31,33], from a helical state at zero field (low susceptibility) to a canted conical state (high susceptibility), to a skyrmion lattice (low susceptibility), back to the canted conical state (high susceptibility), and, finally, to a field-polarized state (low susceptibility). The phase boundaries between these phases are found at the inflection points, which may conveniently be identified as local maxima and minima in the field derivative of the susceptibility, i.e., AC $d\chi/dH$ [Fig. 3(e)] or DC d^2M/dH^2 [Fig. 3(c)]. Below about 222 K, the transitions in and out of the skyrmion lattice phase [called H_{A1} and H_{A2} in Figs. 3(c) and 3(e)] disappear, but the transitions from helical to conical (H_{C1}) and conical to field polarized (H_{C2}) remain. Above $T = 230$ K, only H_{C2} is observed.

When these features are plotted on temperature and field axes, a magnetic phase diagram that is consistent with the phase diagram of other chiral cubic skyrmion host materials is obtained [Fig. 3(f)]. This generically observed diagram features a helical ground state that transforms into a canted conical phase and eventually a field-polarized ferromagnetic phase upon application of field. Just below the Curie temperature, an "A-phase" pocket, which is expected to host a skyrmion lattice structure, is found. In $FePtMo_3N$, this pocket is found between 10 and 20 mT, and 222 and 230 K. At 230 K, a Brazovskii transition is found, which involves a line of first-order transitions from the ordered chiral phases to a short-range ordered "fluctuation-disordered" phase [9,34,35] that persists to 233.5 K. The data points determining the phase boundaries from DC and AC magnetic measurements are in good agreement.

Magnetic phase diagrams constructed from AC susceptibility measurements of the compounds with $x = 0.5$ and $x = 0$
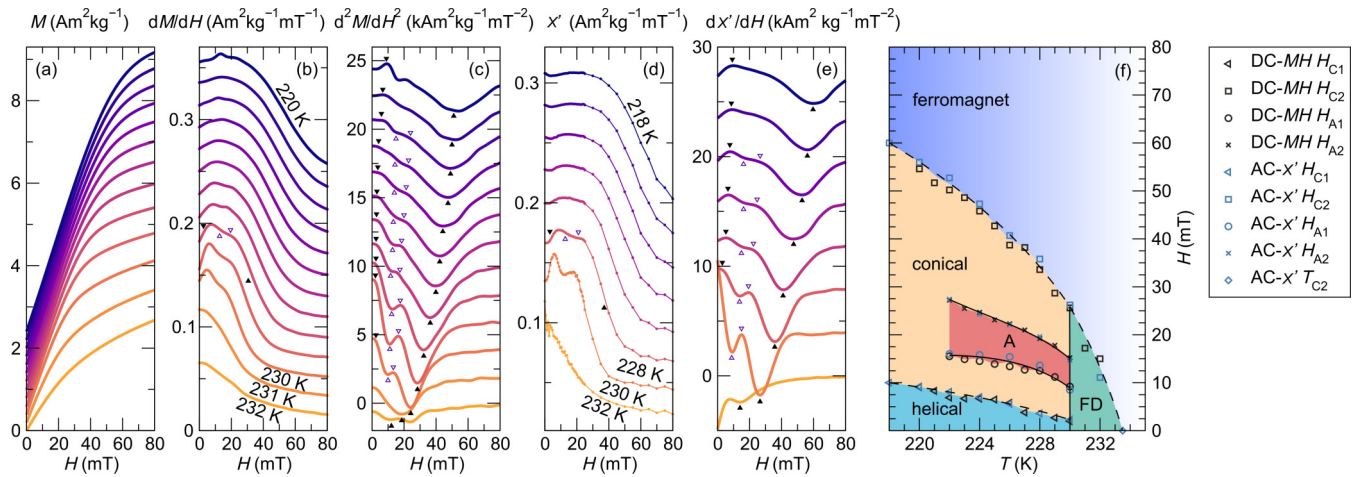
FIG. 3. Magnetic characterization of FePtMo$_3$N. (a) Magnetization vs magnetic field. For visual clarity, the curves are each offset by 0.2 Am^{2}kg^{-1}. (b) dM/dH with an offset between the curves of 0.02 Am^{2}kg^{-1}mT^{-1}. (c) d^2M/dH^2 shifted by 2 kAm^{2}kg^{-1}mT^{-2}. (d) χ' with an offset of 0.01 Am^{2}kg^{-1}mT^{-1} and (e) $d\chi'/dH$ shifted by 4 kAm^{2}kg^{-1}mT^{-2}. The (c) d^2M/dH^2 curves and (e) $d\chi'/dH$ below the magnetic transition temperature show features corresponding to magnetic phase transitions, which can be used to draw a phase diagram in (f). The proposed skyrmionic pocket (A) is shown in red. Solid lines represent first-order phase transitions. The dashed lines represent continuous transitions. FD: fluctuation disordered.

can be found in Fig. 4. Both compounds exhibit signatures similar to FePtMo$_3$N. Skyrmion lattice pockets (A) are observed below the fluctuation-disordered (FD) state starting at 190 K ($x = 0.5$) and 166 K ($x = 0$). The lower temperatures for the A regions correspond to the lower Curie transition temperatures of the compounds. Additionally, the A regions emerge at lower magnetic fields.

Another way of looking at the magnetic phase diagram of the magnetic skyrmion host is on the basis of magnetoentropic mapping, as was previously used to reveal bulk entropy changes associated with magnetic phase transitions in the chiral cubic skyrmion host FeGe [31]. Using the fact that the temperature derivative of magnetization is equal to the field derivative of entropy [Eq. (1)], magnetization vs
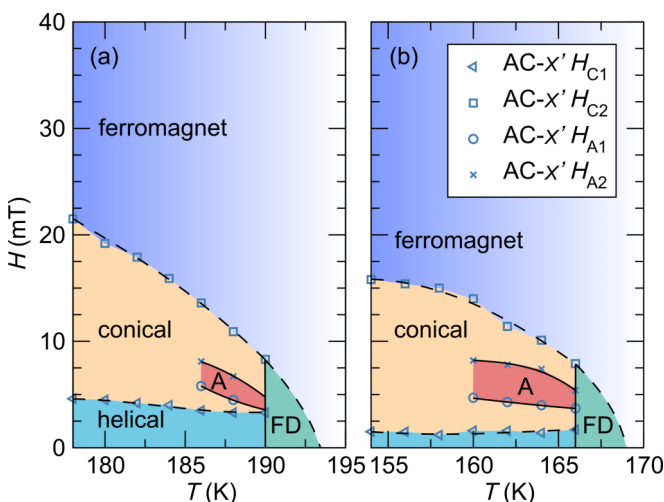
temperature measurements collected at many fields are used to create a map of the entropic response to the field of the sample (Fig. 5). In $M(T)$ measurements of FePtMo$_3$N in low magnetic fields (e.g., 5 mT), a characteristic cusp right below the Curie transition is apparent, shown with an asterisk in Fig. 5(a). When the derivative of this $M(T)$ curve is taken, the cusp becomes a region of positive dS/dH [Fig. 5(b)]—i.e.,

FIG. 4. Magnetic characterization of (a) FePd$_{0.5}$Pt$_{0.5}$Mo$_3$N and (b) FePdMo$_3$N. $d\chi'/dH$ has been used to construct the phase diagrams. The proposed skyrmionic pocket (A) is shown in red. Solid lines represent first-order phase transitions. The dashed lines represent continuous transitions. FD: fluctuation disordered.
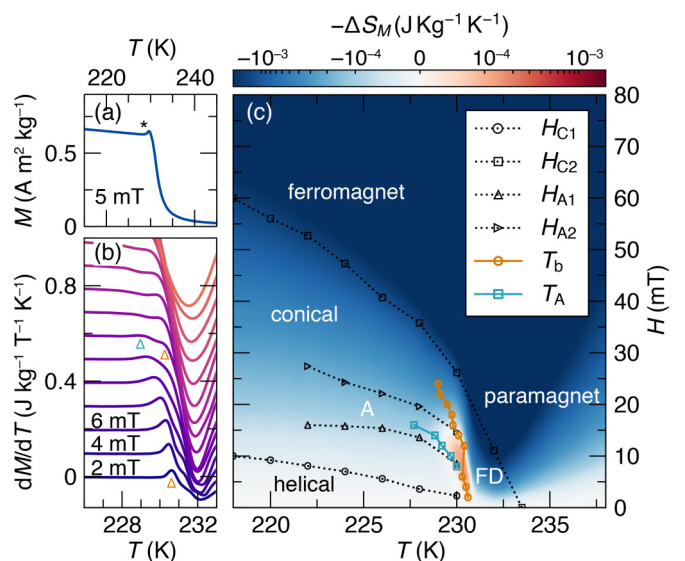

FIG. 5. Magnetoentropic characterization of FePtMo$_3$N. (a) Magnetization vs temperature shows precursor anomalies characteristic for skyrmion host materials, which are seen as features in (b) $dM/dT = dS/dH$. In (b), the orange triangles indicate the anomaly corresponding to the Brazovskii transition, and the teal to the transition from the conical to A state. The curves are offset from each other by 0.1 J kg^{-1} K^{-1} T^{-1} for clarity. (c) Map of the magnetocaloric effect (ΔS_M) with the features from dM/dT indicated as orange and teal lines. The phase transition lines from AC magnetic measurements are shown as black dotted lines.

application of a magnetic field *increases* the entropy of the system. In a skyrmion host material, this counterintuitive phenomenon occurs both at the field-driven conical to skyrmion lattice transition (H_{A1}) and at the Brazovskii transition, where the field drives the transformation from ordered phases to the fluctuation-disordered phase. For most other cases, application of a magnetic field decreases entropy by suppressing spin fluctuations. By tracking the positions of the maxima in dS/dH, phase boundaries of these phase transitions can be determined.

Figure 5(c) shows a map of the isothermal magnetic entropy changes $\Delta S_M(T, H)$ of FePtMo$_3$N, overlaid with the phase diagram determined using AC susceptibility. $\Delta S_M(T, H)$ is the integral with a field of dS/dH [Eq. (2)]. In this map, red regions indicate increased entropy relative to the zero-field state, and blue indicates decreased entropy. The orange and teal points (T_b and T_A) represent the maxima in dS/dH, and generally agree with the position of the Brazovskii transition and the transition from the conical state to the A phase determined using AC susceptibility, although the feature associated with T_A is very subtle and is not resolvable below 227 K. We attribute this weak signal to the polycrystalline nature of the samples: because this technique measures the bulk entropic response of the sample, grain boundaries and defects that do not host the ordered skyrmion lattice phase will weaken the observed bulk entropy signal and contribute a net negative signal as the applied field decreases the spin disorder at these features. For comparison, the magnitude of the positive magnetoentropic signals seen here is about five times less than were observed in single crystals of FeGe [31], but is comparable to that seen in a polycrystalline sample of the skyrmion host Co$_8$Zn$_9$Mn$_3$ [16]. Despite this weakened signal, close to T_C a pocket of increased entropy (the red area in the ΔS_M map) is resolvable, indicating the formation of a phase with higher entropy than the helical ground state. This increased bulk entropy signal is consistent with the formation of a bulk skyrmion lattice phase in the A phase region.

D. Effect of spin-orbit coupling on magnetic exchange and Dzyaloshinskii-Moriya interaction

While the phase diagrams for $x = 0$, 0.5, and 1 are qualitatively the same, the details of the temperatures and fields are expected to be controlled primarily by the ferromagnetic exchange stiffness (A) and Dzyaloshinskii-Moriya interaction densities (D). Furthermore, the helimagnetic wavelength and skyrmion lattice parameter are expected to be related to these constants according to $\lambda = 2\pi A/D$. Here, we use the determined magnetic phase diagrams to obtain estimates for A and D (and therefore the skyrmion lattice parameter) as a function of Pt content x.

First, the observed Curie temperature is used to obtain A. A Monte Carlo investigation of the phase diagram of the Heisenberg model for a cubic chiral magnet [36] has determined that the observed magnetic transition temperature (specifically, the temperature of the Brazovskii transition) is

$$T_C = \frac{J}{0.93 \, k_B}, \tag{3}$$

TABLE III. Ferromagnetic exchange energy J, spin s at 2 K, ferromagnetic exchange stiffness A, DM interaction density D, and expected helical wavelength λ for the series of compounds.

x	J $(10^{-21}$ J$)$	s	A $(10^{-12}$ J m$^{-1})$	D $(10^{-4}$ J m$^{-2})$	λ (nm)
0	2.25	0.60	3.56	1.42	157
0.25	2.37	0.55	3.21	1.68	120
0.5	2.57	0.54	3.26	1.88	109
0.75	2.82	0.52	3.35	2.20	96
1	3.08	0.51	3.48	3.35	65

where J is an effective exchange energy (units of eV) and k_B is the Boltzmann constant. In a cubic system, this exchange energy can be converted to an exchange density A (units of eV nm^{-1}) using

$$A = \frac{Js^2}{a}n, \tag{4}$$

where a is the lattice parameter and n is the coordination number (3 for the 8c site in the present structure) [37]. s is the spin value of the magnetic lattice, which in this case we take to be the average spin value of an atom on the 8c lattice, which is half occupied by magnetic Fe and half by nonmagnetic Pd/Pt. This value is determined using the 2 K saturated magnetization.

The field at which the conical phase saturates to a ferromagnetic state (H_{C2}) can then be used to determine D. If one ignores magnetocrystalline anisotropy, which is believed to be small due to the low helical to conical transition fields observed, then H_{C2} is expected to occur at

$$\frac{\gamma \hbar}{V_0}\mu_0 H_{C2} = \frac{D^2 \sigma(T)}{A}, \tag{5}$$

where V_0, γ, $\hbar$, and μ_0 are the volume of the formula unit cell, the gyromagnetic ratio, the reduced Planck constant, and the vacuum permeability, respectively [17,38]. $\sigma(T)$ is the spin density at a given temperature. In this picture, the temperature dependence of the ordered magnetic moment drives the temperature dependence of H_{C2}. This spin density is obtained from the spontaneous ordered magnetic moment $M_s(T)$ according to

$$\sigma(T) = \frac{M_s(T)V_0}{\gamma \hbar}. \tag{6}$$

M_s at each temperature is deducted from the Arrot-Belov plot (Fig. S2 of the Supplemental Material [32]) [39–41]. For each sample, six $M(H)$ sweeps with a spacing of 2 K were performed below the Curie temperature. Linear fits to the data with values of H/M above 0.05 T kg A^{-1}m^{-2} were used to determine the M_s values from the x intercepts. The parameter D was obtained by Eq. (5) using six values each for H_{C2} and $\sigma(T)$ below the Brazovskii transition. Table III shows J, s, A, D and the helical wavelength λ for the compounds of the series. We note that the approximations made during this analysis, such as the conversion factor between T_C and J, and neglecting the anisotropy terms may lead to errors in the obtained J and D parameters. In particular, neglecting anisotropy may cause a slight overestimation of D and therefore a small underestimation in λ. However, we do not expect
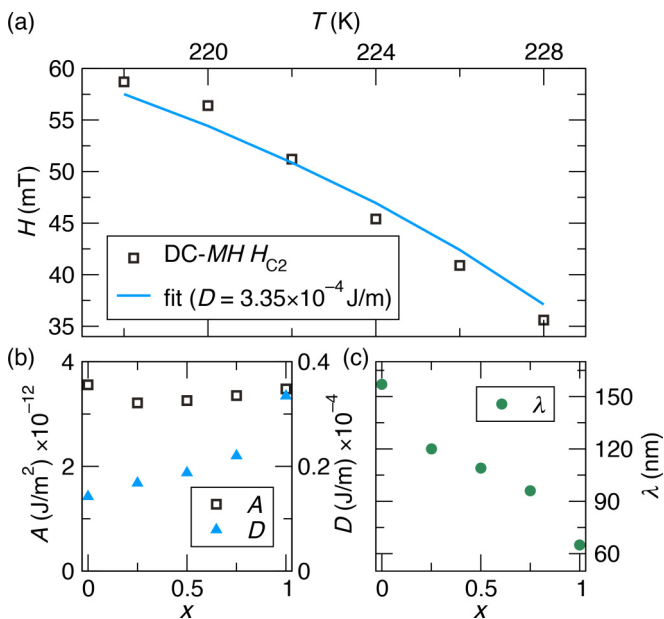
FIG. 6. (a) Values of H_{C2} for $FePtMo_3N$ below the Brazovskii transition and the fit used to obtain the parameter D using Eq. (5) and the values for $S(T)$. (b) Exchange stiffness A and DM interaction density D vs the composition of the series x. (c) Helical wavelengths λ against x.

that the overall trends, especially with regard to expected helical wavelength λ will change. In addition, the calculated values for λ are consistent with those observed for iron cobalt rhodium molybdenum nitride [27].

Figure 6(b) shows the change of A and D with the variation of the composition x. The exchange stiffness A generally increases slightly with increasing x, which corresponds to the increasing Curie temperatures. The value for the $x = 0$ sample differs from the trend of the series due to the higher s value. Overall, A only changes by about 10% across the series. On the other hand, the parameter D is found to increase dramatically with rising x, increasing by 235% across the series. Therefore, we conclude that the introduction of heavy Pt atoms enhances the strength of spin-orbit coupling and therefore DM interaction. This increase is also visible in Fig. 2(a), where the larger DM interactions lead to bigger saturation fields and therefore to a smaller susceptibility in the low-field magnetic measurements for the compounds with higher Pt content. As a result of the increasing DM interaction strength, the helical period length λ [Fig. 6(c)] and the skyrmion lattice parameter are expected to decrease from 157 nm for $x = 0$ to 65 nm for $x = 1$. The increase in spin-orbit coupling also causes the fields needed to stabilize the skyrmions to increase from about 50 mT for $x = 0$ to about 150 mT for $x = 1$. The proposed skyrmion lattice phases in the polycrystalline nitride samples are with their expected lattice parameters ranging between 50 and 150 nm suitable for direct observation using small-angle neutron scattering [42] or Lorentz transmission electron microscopy [27].

The expected wavelengths λ for the compounds in the series $FePd_{1-x}Pt_xMo_3N$ are comparable to that observed in the near-room-temperature skyrmion host FeGe ($T_C = 278$ K,

$\lambda = 70$ nm) [11]. On the other hand, much smaller skyrmions have been observed in MnSi (18 nm) [3]; however, this small skyrmion size can be largely attributed to the small ferromagnetic exchange constant, as evidenced by the low $T_C = 29$ K. On the other hand, $Co_xZn_yMn_z$, which can show a stable skyrmion lattice at high temperature (between 150 to 475 K, depending on composition), shows larger skyrmion lattice parameters of between 115 and 190 nm [12]. In the room-temperature antiskyrmion host $Mn_{1.4}PtSn$, the lattice parameter ranges from about 150 to 350 nm depending on temperature and field [43]. An interesting feature in our nitrides is that the skyrmion size can be decreased while simultaneously increasing the Curie temperature. The skyrmion size is reduced by more than 50% going from $FePdMo_3N$ to $FePtMo_3N$, while the Curie temperature is simultaneously increased by 65 K. In the compounds $Co_xZn_yMn_z$ ($x + y + z = 20$), the change in composition from $Co_9Zn_9Mn_2$ to $Co_8Zn_8Mn_4$ decreases the helical period length from 155 to 125 nm, but also decreases T_C from 425 to 310 K. Similar behavior can be seen in the skyrmion hosts $Mn_{1-x}Ir_xSi$ and $Fe_{1-x}Mn_xGe$, where the decrease of λ also leads to significant reduction in T_C [21,22].

IV. CONCLUSION

We have shown that $FePd_{1-x}Pt_xMo_3N$ compounds in the filled β-Mn crystal structure are promising bulk skyrmion host candidates. High-purity polycrystalline samples with different Pd/Pt ratios can be made in a simple gas nitridation procedure, followed by an annealing step under pressurized nitrogen. DC magnetization and AC susceptibility measurements reveal that these compounds exhibit magnetic phase diagrams consistent with those of other chiral cubic skyrmion hosts. In $FePtMo_3N$, an A phase below 230 K with a width of 8 K and a height of 10 mT is seen. The magnetic phase diagrams of these compounds are used to determine the ferromagnetic exchange stiffness A and Dzyaloshinskii-Moriya interaction density D for each of the compounds. This analysis indicates that D increases with increasing Pt content and, consequently, the skyrmion lattice parameter is predicted to be tunable between 157 nm ($x = 0$) and 65 nm ($x = 1$). This study demonstrates that the introduction of heavy elements into a skyrmion host can be used to control D and achieve small skyrmions; however, for this strategy to be effective, the substitution must be performed in such a way as to not weaken the ferromagnetic exchange.

[1] C. Felser, Angew. Chem. Int. Ed. **52**, 1631 (2013).

[2] A. Fert, V. Cros, and J. Sampiano, Nat. Nanotechnol. **8**, 152 (2013).

[3] S. Mühlbauer, B. Binz, F. Jonietz, C. Pfleiderer, A. Rosch, A. Neubauer, R. Georgi, and P. Böni, Science **323**, 915 (2009).

[4] W. Münzer, A. Neubauer, T. Adams, S. Mühlbauer, C. Franz, F. Jonietz, R. Georgii, P. Böni, B. Pedersen, M. Schmidt, A. Rosch, and C. Pfleiderer, Phys. Rev. B **81**, 041203(R) (2010).

[5] X. Z. Yu, Y. Onose, N. Kanazawa, J. H. Park, J. H. Han, Y. Matsui, N. Nagaosa, and Y. Tokura, Nature (London) **465**, 901 (2010).

[6] A. Bogdanov and A. Hubert, J. Magn. Magn. Mater. **138**, 255 (1994).

[7] I. Dzyaloshinskii, J. Phys. Chem. Solids **4**, 241 (1958).

[8] T. Moriya, Phys. Rev. **120**, 91 (1960).

[9] A. Bauer and C. Pfleiderer, Generic aspects of skyrmion lattices in chiral magnets, in *Topological Structures in Ferroic Materials*, Springer Series in Materials Science, Vol. 228, edited by J. Seidel (Springer, Cham, 2016), pp. 1–28.

[10] A. Bauer and C. Pfleiderer, Phys. Rev. B **85**, 214418 (2012).

[11] X. Z. Yu, N. Kanazawa, Y. Onose, K. Kimoto, W. Z. Zhang, S. Ishiwata, Y. Matsui, and Y. Tokura, Nat. Mater. **10**, 106 (2011).

[12] Y. Tokunaga, X. Z. Zu, J. S. White, H. M. Rønnow, D. Morikawa, Y. Taguchi, and Y. Tokura, Nat. Commun. **6**, 7638 (2015).

[13] K. Karube, J. S. White, D. Morikawa, M. Bartkowiak, A. Kikkawa, Y. Tokunaga, T. Arima, H. M. Rønnow, Y. Tokura, and Y. Taguchi, Phys. Rev. Materials **1**, 074405 (2017).

[14] K. Karube, J. S. White, D. Morikawa, C. D. Dewhurst, R. Cubitt, A. Kikkawa, X. Yu, Y. Tokunaga, T. Arima, H. M. Rønnow, Y. Tokura, and Y. Taguchi, Sci. Adv. **4**, eaar7043 (2018).

[15] R. Ritz, M. Halder, C. Franz, A. Bauer, M. Wagner, R. Bamler, A. Rosch, and C. Pfleiderer, Phys. Rev. B **87**, 134424 (2013).

[16] J. D. Bocarsly, C. Heikes, C. M. Brown, S. D. Wilson, and R. Seshadri, Phys. Rev. Materials **3**, 014402 (2019).

[17] M. Kataoka, J. Phys. Soc. Jpn. **56**, 3635 (1987).

[18] M. Heide, G. Bihlmayer, and S. Blügel, Physica B **404**, 2678 (2009).

[19] U. K. Rößler, A. A. Leonov, and A. N. Bogdanov, J. Phys.: Conf. Ser. **303**, 012105 (2011).

[20] A. Soumyanarayanan, M. Raju, A. L. Gonzales Oyarce, A. K. C. Tan, M.-Y. Im, A. P. Petrović, P. Ho, K. H. Khoo, M. Tran, C. K. Gan, F. Ernult, and C. Panagopoulos, Nat. Mater. **16**, 898 (2017).

[21] C. Dhital, L. DeBeer-Schmitt, Q. Zhang, W. Xie, D. P. Young, and J. F. DiTusa, Phys. Rev. B **96**, 214425 (2017).

[22] K. Shibata, X. Z. Yu, T. Hara, D. Morikawa, N. Kanazawa, K. Kimoto, S. Ishiwata, Y. Matsui, and Y. Tokura, Nat. Nanotechnol. **8**, 723 (2013).

[23] T. J. Prior and P. D. Battle, J. Solid State Chem. **172**, 138 (2003).

[24] T. J. Prior, D. Nguyen-Manh, V. J. Couper, and P. D. Battle, J. Phys.: Condens. Matter **16**, 2273 (2004).

[25] T. J. Prior, S. E. Oldham, V. J. Couper, and P. D. Battle, Chem. Mater. **17**, 1867 (2005).

[26] P. D. Battle, F. Grandjean, G. J. Long, and S. E. Oldham, J. Mater. Chem. **17**, 4785 (2007).

[27] W. Li, C. Jin, R. Che, W. Wei, L. Lin, L. Zhang, H. Du, M. Tian, and J. Zang, Phys. Rev. B **93**, 060409(R) (2016).

[28] J. O. Conway and T. J. Prior, J. Alloys Compd. **774**, 69 (2019).

[29] P. W. Stephens, J. Appl. Crystallogr. **32**, 281 (1999).

[30] J. J. Stickel, Comput. Chem. Eng. **34**, 467 (2010).

[31] J. D. Bocarsly, R. F. Need, R. Seshadri, and S. D. Wilson, Phys. Rev. B **97**, 100404(R) (2018).

[32] See Supplemental Material at http://link.aps.org/supplemental/10.1103/PhysRevMaterials.4.024412 for x-ray fluorescence compositional analysis data, differential scanning calorimetry data, and additional data pertaining to the determination of the Dzyaloshinskii-Moriya interaction density from the magnetic phase diagrams.

[33] T. Adams, A. Chacon, M. Wagner, A. Bauer, G. Brandl, B. Pedersen, H. Berger, P. Lemmens, and C. Pfleiderer, Phys. Rev. Lett. **108**, 237204 (2012).

[34] M. Janoschek, M. Garst, A. Bauer, P. Krautscheid, R. Georgii, P. Böni, and C. Pfleiderer, Phys. Rev. B **87**, 134407 (2013).

[35] S. A. Brazovskii, Zh. Eksp. Teor. Fiz. **68**, 175 (1975) [Sov. Phys. JETP **41**, 85 (1975)].

[36] S. Buhrandt and L. Fritz, Phys. Rev. B **88**, 195137 (2013).

[37] S. Chikazumi, *Physics of Ferromagnetism* (Oxford University Press, New York, 1997).

[38] M. N. Wilson, A. B. Butenko, A. N. Bogdanov, and T. L. Monchesky, Phys. Rev. B **89**, 094411 (2014).

[39] K. P. Belov and A. N. Goryaga, Fiz. Met. Metalloved. **2**, 3 (1956).

[40] A. Arrot, Phys. Rev. **108**, 1394 (1957).

[41] D. Kuz'min, D. Givord, and V. Skumryev, J. Appl. Phys. **107**, 113924 (2010).

[42] D. A. Gilbert, A. J. Grutter, P. M. Neves, G.-J. Shu, G. Zimanyi, B. B. Maranville, F.-C. Chou, K. Krycka, N. P. Butch, S. Huang, and J. A. Borchers, Phys. Rev. Materials **3**, 014408 (2019).

[43] A. K. Nayak, V. Kumar, T. Ma, P. Werner, E. Pippel, R. Sahoo, F. Damay, U. K. Rößler, C. Felser, and S. S. P. Parkin, Nature (London) **548**, 561 (2017).